Chemical Engineering Journal 503 (2025) 158137

Contents lists available at ScienceDirect

Chemical Engineering Journal

journal homepage: www.elsevier.com/locate/cej

Cucurbit[6]uril-tuned nanochannels of graphene oxide membrane for enhanced water flux in nanofiltration

Pengfei Yang [a,e,f], Yanan Liu [a,b,e], Gowan-Hugh Whalley [a,e], Chengzhi Guo [a,e,f], Ya Li [c,d], A.Ozgur Yazaydin [e], Zhongyi Jiang [b,c,d,*], Marc-Olivier Coppens [a,e], Yang Lan [a,e,f,*]

[a] Centre for Nature-Inspired Engineering, Department of Chemical Engineering, University College London, Gower Street, London WC1E 7JE, United Kingdom
[b] Department of Chemistry and Chemical Engineering, Hainan University, No. 58, Renmin Road, Haikou 570228, China
[c] Key Laboratory for Green Chemical Technology of Ministry of Education, Department of Chemical Engineering and Technology, Tianjin University, No. 92, Weijin Road, Tianjin, 300072, China
[d] Collaborative Innovation Centre of Chemical Science and Engineering (Tianjin), Tianjin University, No. 92, Weijin Road, Tianjin 300072, China
[e] Department of Chemical Engineering, University College London, Gower Street, London WC1E 7JE, United Kingdom
[f] Manufacturing Futures Lab, Department of Chemical Engineering, University College London, London, United Kingdom

ARTICLE INFO

Keywords:
Nanofiltration membrane
Cucurbit[6]uril
Graphene oxide
Dye/salt separation
Wastewater treatment

ABSTRACT

Graphene oxide (GO) membranes exhibit promising potential in nanofiltration due to their controllable transport channel size and low transport resistance of water molecules, resulting in exceptional water permeability. However, the trade-off between water flux and rejection ratio stemming from tightly packed interlayers poses a challenge to the application of GO membranes in nanofiltration. To overcome this trade-off, a practical method is urgently needed to regulate the interlayer space of GO membranes. In this study, a macrocyclic molecule with a rigid porous structure, cucurbit[6]uril (CB[6]), has been introduced to enlarge and precisely adjust the interlayer distance of GO membranes, effectively addressing the trade-off dilemma. The interlayer distance can be precisely adjusted within a range of 0.46 to 1.35 nm, making it suitable for the removal of small organic molecules from wastewater. Through the optimization of GO and CB[6] quantities, the GO membrane containing 20 μg GO and 49.9 wt% CB[6] (CB6GO-4) demonstrates a high pure water flux (PWF) exceeding 171.3 L $m^{-2}h^{-1}$ bar^{-1}, more than 5.9 times higher than a pure GO membrane (28.8 L $m^{-2}h^{-1}$ bar^{-1}), alongside a dye rejection ratio over 92 %, indicating the promising potential of CB[6]-intercalated GO membranes in removing organics from industrial saline wastewater.

1. Introduction

There exists a pressing necessity to treat wastewater containing salt ions and organic pollutants, notably dyes, due to global water scarcity and escalating environmental concerns [1–4]. A viable approach for wastewater treatment involves nanofiltration utilizing membranes with pore sizes ranging from 0.5 nm to 2.0 nm, because of its high separation efficiency and low energy consumption [5–8]. Graphene oxide (GO) is extensively employed in the research of nanofiltration membranes due to its suitable transport channel size, minimal transport resistance to small molecules, and excellent stability [9–18]. However, the water flux through pure GO membrane is constrained by the tightly packed GO nanosheets. To improve water flux in GO membranes, it is imperative to increase the interlayer distance, yet this expansion must be carefully managed to maintain a balance between membrane permeance and rejection ratio. Thus, to achieve optimum efficiency in wastewater purification, it is crucial to precisely control the expansion of the interlayer to meet specific separation requirements [19–23].

In order to develop a GO-based nanofiltration membrane with both high water flux and effective separation capabilities, extensive research efforts have been devoted to manipulating the physical or chemical environments of the transport channels within the GO-based membrane. One approach involves the modification of GO with functional groups to increase the hydrophilicity of the GO surface to facilitate water transport [12]. Another strategy focuses on engineering specific structures on the GO surface to widen the interlayer spacing and reduce water transport resistance [24,25]. Moreover, incorporating perforations or punch holes on the GO can help shorten the length of water transport pathways

* Corresponding author.
E-mail addresses: zhyjiang@tju.edu.cn (Z. Jiang), yang.lan@ucl.ac.uk (Y. Lan).

https://doi.org/10.1016/j.cej.2024.158137
Received 16 August 2024; Received in revised form 28 October 2024; Accepted 28 November 2024
Available online 29 November 2024

[26,27]. While these methods aid in achieving a balance between flux and selectivity, the synthesis processes associated with these approaches are intricate and challenging to control. As an alternative, a more straightforward method involves intercalating various nanomaterials, including ions [28], metallic oxides [29,30], quantum dots [31], nanotubes [11,32], nanorods [33], 2D nanosheets [12,34] and 3D nanoparticles [35] into the interlayers of GO nanosheets. This intercalation enables precise control of the interlayer distance to attain the desired separation properties. Nevertheless, obstacles remain, such as intercalator self-aggregation, intercalator loss, due to weak interactions with the GO, and uneven distribution of the intercalators. An ideal intercalator would not only finely adjust the interlayer distance to a specific value but also remain stable and uniformly distributed across the GO surface. To efficiently remove dyes from wastewater containing salt ions and organic waste, it is crucial to identify a nanomaterial capable of optimally adjusting the GO interlayer distance between the diameter of salt ions and the dye molecules. Macrocycles are emerging as a significant material in the development of highly accurate molecular sieving membranes, owing to their well-defined cavities that can be effectively utilized as membrane pores to enhance separation performance [36,37]. Jiang et al. have demonstrated this potential by aligning amino-functionalized macrocycles, specifically cyclodextrins, within ultrathin nanomembranes. This alignment creates well-defined sub-nanometre pores for membranes that not only achieve double the methanol permeance compared to their disordered counterparts but also exhibit superior selectivity. Moreover, these aligned macrocycle membranes significantly outperform commercial membranes in the enrichment of cannabidiol oil, showcasing an order of magnitude faster ethanol transport and a threefold increase in enrichment efficiency [37].

Cucurbit[n]urils (CB[n]s), characterized by their rigid, hollow, pumpkin-like cage structures, represent a distinct category of macrocyclic molecules [38]. Particularly, cucurbit[6]uril (CB[6]), featuring an outer diameter of 1.44 nm and a height of 0.91 nm, demonstrates suitability as an intercalator in nanofiltration membranes due to its size and structural rigidity [39]. Unlike other intercalators, CB[n]s have shown strong interaction with 2D nanosheets due to the carbonyl groups at each ends of the portals, making them hard to peel off [40]. Moreover, Their hydrophobic cavities can potentially provide pathways for the rapid transport water molecules to further facilitate the water flux [41]. These properties enable CB[6] to inhibit the packing of GO interlayer channels, thereby preserving channel size during the filtration processes [42,43]. The capability of CB[6] to adjust channel size in nanofiltration membranes has already been documented by several researchers [44–48]. For instance, Sun et al. have developed a CB[6]-hybridized dendritic polyamidoamine nanofiltration membrane. The integration of CB[6] leads to the expansion of polyamide tunnels, facilitated by the large steric hindrance of CB[6] and hydrophobic rotaxane tunnels that arise from the host–guest chemistry between CB[6] and piperazine (PIP), consequently enhancing water flux. The augmentation in water flux correlates with the CB[6] loading content, underscoring the critical role of CB[6] in enhancing membrane efficiency [45].

In this study, the investigation focuses on the utilization of CB[6] as an intercalator for the regulation of interlayer spacing in GO membranes. CB[6] molecules are introduced into the interlayer region using a vacuum-assisted self-assembly approach, enabling precise control over the dimensions of the water transport channels. The resulting membranes are denoted as CB6GO-X, where X ranges from 1 to 5, representing the progressive increase in the proportion of CB[6] within the sample membrane. Through the vacuum filtration process, the alignment of GO nanosheets is facilitated, driven by the π-π stacking interactions, facilitating the establishment of long-range and ordered water pathways. By varying the CB[6] content, the CB6GO-X membranes achieve both high pure water flux (PWF) and dye rejection ratio. This performance is ascribed to the meticulous adjustment of the interlayer distance, supported by X-ray diffraction (XRD) measurements and molecular dynamics simulations. Furthermore, the membranes demonstrate high selectivity for dye over salt; the increased interlayer distance permits the passage of hydrated salt ions through the membrane, showcasing the potential of CB6GO-X membranes in purifying organic compounds from industrial saline wastewater.

2. Materials and methods

2.1. Materials and reagents

All reagents were commercially available and used without further treatment. Polyethersulfone (PES) microfiltration membrane (pore size = 0.22 μm) was purchased from Hangzhou Special Paper Industry Co., Ltd (Hangzhou, China). Waterman Anodisc^{TM} 47 microfiltration membrane (pore size = 0.22 μm) was purchased from GE Healthcare company. Urea (>99.7%), glyoxal (40 wt.% in H_2O), and paraformaldehyde (95%) were purchased from Meryer Chemical Reagent Co., Ltd. (Shanghai, China). Hydrochloric acid (38 wt.%), ethanol (>99.5%) and acetone (>99.5%) were purchased from Yuanli Chemical Reagent Co., Ltd (Tianjin, China). Alcian blue, Congo red, Eriochrome Black T and Methyl blue were purchased from Aladdin Industrial Co. (Shanghai, China). Sodium sulfate (Na_2SO_4, >99.0%), magnesium sulfate ($MgSO_4$, >99.0%), magnesium chloride ($MgCl_2$, >99.0%) and sodium chloride (NaCl, >99.0%) were purchased from Jiangtian Chemical Reagent Co., Ltd. (Tianjin, China). Deionized water used in all experiments was produced by a reverse osmosis unit.

2.2. Synthesis of cucurbit[6]uril (CB[6])

300 g urea was dissolved in 500 mL water. 250 g 40 % aq. glyoxal solution, 43 mL 12 M concentrated HCl was mixed with the urea solution in a flask. The mixed solution was heated at 85 °C until a heavy precipitate formed. The reaction mixture was filtered after it cooled down to room temperature. The filter cake was washed with deionized water and acetone several times. The resulting white solid was dried under vacuum at room temperature for 24 h. The white powder was glycoluril.

The glycoluril was mixed with paraformaldehyde in a flask. 260 mL ice-cold concentrated HCl solution was added to the mixed powder at a slow rate under stirring. After the addition of approximately 100 mL of concentrated HCl, the mixture became unresponsive to stirring, solidifying into a brick-like material. The heterogeneous mixture was gradually heated to 80 °C in 2.5 h and maintained at 80 °C for another 4 h at which point all the solids dissolved. The homogenous red solution was heated to 100 °C and kept for 19 h. After the reaction, the mixed solution was poured out and cooled down to room temperature. The product was gently poured into 2.5 L of ethanol while stirring the solution. After 12 h of continuous stirring, the CB[n] completely precipitated. The mixture was filtered, and the precipitate was collected in a flask. It was then washed with ethanol and acetone three times until the pH reached 7. The crude CB[n] was subsequently dried in a vacuum oven at room temperature for 24 h.

Following this, 3 L of deionized water were added to the crude CB[n]. This resulted in the dissolution of CB[5] and CB[7] into the water, while CB[6] and CB[8] remained in solid form. The mixture was subjected to filtration, and the precipitate, which contained CB[6] and CB[8], was then stirred in 3 M HCl. This process allowed for the isolation of CB[8] as an insoluble solid. The solution containing CB[6] in 3 M HCl was subsequently concentrated using the rotary evaporation method, resulting in the precipitation of CB[6]. The solid CB[6] was then recrystallized from warm concentrated HCl multiple times to obtain pure CB[6]. The pure CB[6] was washed with ethanol and acetone and subsequently dried in a vacuum oven for 24 h.

2.3. Synthesis of graphene oxide (GO)

Graphene oxide (GO) was synthesized using a modified Hummer method [43]. Initially, 5 g of graphite flake powder and 2 g of $NaNO_3$

were mixed in a beaker. This mixture was then slowly introduced into a three-necked flask containing 125 mL of concentrated H_2SO_4, all the while being stirred at 0 °C. Subsequently, 30 g of $KMnO_4$ were slowly added to the mixture with continuous stirring at 0 °C. This step in the procedure took approximately half an hour. Once the addition of $KMnO_4$ was completed, the temperature was raised to 35 °C, and the mixture was stirred at this temperature for an additional half-hour. Subsequently, 250 mL of deionized water was introduced into the flask. The temperature was further raised to 98 °C, and the solution was stirred at 98 °C for an additional 3 h. After the reaction, a sufficient amount of H_2O_2 was added to the mixture to remove the unreacted $KMnO_4$. Finally, the mixture was washed with 1 L 1 M HCl and then it was washed with water until the pH reached 7. A certain amount of GO aqueous was taken out and dried via vacuum freezing and drying. Then, some GO powder was weighted and diluted with water to 20 μg mL^{-1} and then treated with ultrasound for 30 min.

2.4. Preparation of CB6GO-X membranes

CB[6] was dissolved in 1 M HCl to make a 25 μg mL^{-1} CB[6] solution. A certain volume of GO solution was transferred to a beaker. Subsequently, a certain amount of deionized water was added to the beaker to dilute the GO solution. The resulting diluted GO solution was subjected to ultrasonication for 5 min. The resulting dispersion was filtered on a polyethersulfone (PES) membrane substrate via the vacuum-assisted filtration method. To determine the optimal amount of GO for the fabrication of CB[6] hybrid GO membranes, a series of GO membranes were produced with varying GO quantities (10 μg, 20 μg, 30 μg, 40 μg, and 50 μg). The results revealed that 20 μg provided the best balance between the pure water flux (PWF) and rejection rate. Therefore, 20 μg was selected as the amount for creating CB6GO-X membranes.

Subsequently, different quantities of CB[6] (5 μg, 10 μg, 15 μg, and 20 μg, 25 μg) solutions were added to the GO, resulting in the formation of CB6GO-X membranes through the same process used for pure GO membranes. The value of X (1, 2, 3, 4 and 5) was assigned according to the order of addition of CB[6] with different amounts.

2.5. Characterization

The operation details of some characterization items can refer to the literature [49–52]. Field emission scanning electron microscopy (FESEM, Nanosem 430, Japan) was used to observe the morphology and thickness of the membrane samples in this work. Energy dispersive X-ray spectroscopy (EDX, Genesis XM2 APEX 60SEM, USA) was used to observe the elemental distribution and the composition of samples in this work. Transmission electron microscopy (TEM, JEM-2100F, Japan) was utilized to observe the nanoscale morphology of the CB[6], GO nanosheets and CB[6]/GO composite in this work. Fourier transform infrared spectroscopy (FTIR, Nicolet 560, USA) was used to characterize the chemical structure of the samples in this work. X-ray photoelectron spectroscopy (XPS, ThermoFisher Scientific, ESCALAB Xi+, UK) was also used to characterize the chemical structure of the samples in this work. X-ray diffraction (XRD, Rigaku D/max 2500 v/pc Cu Kα, Japan) was used to analyse the interlayer distance of the membrane samples in this work. The scanning range extended from 3 to 40 degrees, and the scanning rate was set at 8 degrees per minute. The interlayer space of membrane can be calculated by Bragg's law:$\lambda = 2d\sin(\theta)$, where λ is the wavelength of the X-ray source. For CuKa, λ is 0.154 nm. d (nm) is the interlayer space of the adjacent GO sheets. θ (°) is the diffraction angle. The real CB[6] content of the membranes in this project was calculated from the TGA results. The TGA tests of the membranes were performed by the Mettler Toledo 3 + . The temperature range employed in the experiment spanned from 40 °C to 800 °C under a nitrogen atmosphere. The heating rate was maintained at 10 °C per minute. Ultraviolet–visible spectroscopy (Hitachi UV-3010, Japan) was used to analyse the interaction between the CB[6] and GO nanosheets. The samples for characterizing the interaction between the CB[6] and GO nanosheets were prepared by diluting the solution used to prepare CB6GO-X membranes. The zeta potential of the CB6GO-3 membrane surface was measured by the SurPASS Electrokinetic Analyzer (SurPASS, Austria).

2.6. Molecular dynamics simulations

Molecular dynamics simulations were used to determine the binding conformation of CB[6] to the surface of graphene and predict how CB[6] intercalation would influence the interlayer distance between graphene sheets and the optimal orientation of CB[6] relative to the graphene surface. Several simulations were carried out, considering the interaction of CB[6] with first one, and then two sheets of graphene. These were performed under vacuum with a thermostat set at 300 K with forcefield parameters generated for CB[6] in OPLS-AA using the PolyParGen service with esp charges generated by *ab initio* Hartree-Fock calculation in a STO-3G basis set [53]. This is a forcefield that performed well in previous studies of amino acids adsorbing onto graphene surfaces [54]. To calculate binding energy, energy minimisation was performed on each frame followed by single point energy calculations on first the whole structure and then each individual component. This allowed the identification of the region where CB[6] had equilibrated on/between the surfaces allowing accurate determination of the binding energies and associated errors. Errors were more significant for the system with two graphene layers with greater oscillation in binding energy and interlayer distance at equilibrium than when CB[6] interacted with a graphene surface. Graphene rarely is present in bulk systems as single layers, having a strong tendency for aggregation in both the oxidised and reduced forms [55,56]. As such, graphene sheets were used throughout to simulate a few-layer graphene system [57]. To determine the extent to which this parallel configuration is favoured over the perpendicular binding orientation, simulations were run under the same conditions but with restraints of 100 N applied in the x and y directions to the carbon atoms in the CB[6] backbone.

2.7. Separation performance measurement

The separation performance of the membranes was tested by using a dead-end filtration cell and a crossflow filtration system. For the dead-end filtration cell (model 8010, Millipore Co., USA) with an effective area of 4.1 cm^2 equipped with a magnetic stirrer, the membrane sample was placed at the bottom of the cell. Before the measurement, each membrane sample was pressed with deionized water at 2 bar for a couple of hours until the flux became stable. The rejection performance of the membranes was measured at 1 bar by replacing the deionized water with a different dye solution. The concentration of the dye solution was 100 ppm. The concentration of the salt solution was 1000 ppm. For the dye/salt mixed solution, the concentration of dye and salt was also 100 ppm and 1000 ppm, respectively. For the crossflow filtration, the membrane sample was loaded in a homemade cell with an effective diameter of 1.4 cm. The permeance (J, L $m^{-2}h^{-1}$ bar^{-1}) and rejection ratio (R, %) was calculated from the following equations:

$$J = \frac{V}{A\Delta t\Delta P}$$

$$R = \frac{a_f - a_p}{a_f} \times 100\%$$

where V (L) was the volume of the permeate at a certain time, A (m^2) was the effective membrane area, Δt (h) was the permeating time and ΔP (bar) was the driving pressure, a_f and a_p were the absorbance of the feed solution and permeate solution, respectively.

3. Results and discussion

3.1. Fabrication of the CB[6] intercalated CB6GO-X membranes

The CB[6]-intercalated membranes are designed to adjust interlayer spacing by controlling the concentration of CB[6]. The process and mechanism for tuning the interlayer spacing in CB6GO-X membranes are depicted in Fig. 1. Initially, CB[6] is introduced into a diluted GO solution, where it assembles on GO nanosheets through hydrogen bonding and dipole-π interactions, forming a CB[6]/GO composite. The CB[6]/GO composite is then structured into membranes by a vacuum-assisted self-assembly method. The intercalation of CB[6] expands the compact GO interlayer, as the rigid macrocyclic structure of CB[6] keeps the GO nanosheets apart. This expansion allows the interlayer spacing in CB6GO-X membranes to be accurately controlled by adjusting the amounts of CB[6]. The spacing between two adjacent GO nanosheets functions as channels that facilitate water transport while blocking pollutants, enabling effective water purification.

3.2. Characterization of the membranes

The morphology of the membranes is examined using a scanning electron microscope (SEM), as presented in Fig. 2. The surface analysis of the pure GO membrane reveals a structure free of defects. The ridges observed in the SEM image stem from the stacking of the GO nanosheets along the edges of the substrate pores, with the flat areas representing the coverage of the substrate pores by the GO membrane. Following the intercalation of CB[6], the CB6GO-X membranes maintain a similar surface structure to the pure GO membrane, as shown in Fig. 2b-2e. The thickness of the membranes can be measured from the corresponding cross-sectional SEM images as shown in Fig. 2f-2j. To emphasize the membrane, the substrate is artificially colorized in red (the original SEM figures are shown in Figure S3). In Fig. 2f, the average thickness of the pure GO membrane is 17 nm. The introduction of CB[6] leads to an increased thickness in the CB6GO-X membranes due to the expanded interlayer distance among the GO nanosheets. This thickness progressively increases from 22 nm to 39 nm with an escalation in CB[6] content (Fig. 2g-2j). Additionally, Figure S4 presents the energy dispersive X-ray spectroscopy (EDX) mapping of the nitrogen element in the CB6GO-3 membrane, validating the uniform distribution of CB[6] within the membrane.

The chemical structure of the membranes is verified by Fourier Transform Infrared (FTIR) spectroscopy and X-ray Photoelectron Spectroscopy (XPS) analysis. In the FTIR spectra shown in Fig. 3a, the peak at 1723 cm^{-1} in the spectrum of pure GO membrane is attributed to the stretching vibration of the carboxyl groups (–COOH) of GO, while the peak at 1620 cm^{-1} corresponds to the stretching vibration of the carbon–carbon double bond (−C = C) of GO. Upon the introduction of CB[6], a distinct new peak emerges at 1416 cm^{-1}, indicating the stretching vibration of the carbon–nitrogen bond (−C-N) within CB[6]. Moreover, the transmittance ratio between the peaks at 1723 cm^{-1} and 1620 cm^{-1} increases progressively, reflecting the escalation in CB[6] content. The XPS spectra further validate these findings, with the pristine GO membrane exhibiting no −C-N peak in the C 1 s spectrum, as depicted in Figure S5. Conversely, the −C-N peak appears in the C 1 s spectrum of the CB6GO-3 membrane (Fig. 3b), signifying the successful intercalation of CB[6] into the CB6GO-X membranes.

CB[6] assembles stably on the GO surface, likely due to hydrogen bonds and dipole-π interaction between CB[6] and the GO nanosheets. The interactions between GO nanosheets and CB[6] are further investigated using ultraviolet–visible spectroscopy (UV–vis) spectroscopy. The π electrons of GO are postulated to share atomic orbitals with the electrons from carbonyl groups in CB[6]. As shown in Fig. 4a, the UV–vis absorption peak for GO at 236 nm, associated with the $\pi \rightarrow \pi^*$ transitions for the C = C bonding [58], red-shifts to 239 nm upon the introduction of CB[6]. This shift indicates a slight enhancement in electronic conjugation, potentially due to the dipole-π conjugation between GO and CB[6] [59], enabling stable immobilization of CB[6] on the GO nanosheets surface in water. Additionally, transmission electron microscopy (TEM) observations confirm the morphology of GO nanosheet and CB[6]/GO composite. The GO nanosheet shows a plain, thin, layered structure, as shown in Figure S6. After the addition of CB[6], this layered structure is maintained in the CB[6]/GO, as depicted in Fig. 4b.

As previously stated, the water flux of the GO membrane is restricted by the densely stacked GO nanosheets. To tackle this issue, fine-tuning the interlayer space within these membranes is required. As shown in Fig. 4c, the baseline interlayer space of the GO membrane is 0.46 nm as measured by X-ray diffraction (XRD) and calculated using Bragg's law (Equation S1) [60]. The rigid structure of CB[6], with an outer diameter of 1.44 nm and height of 0.91 nm, facilitates the separation of GO layers,

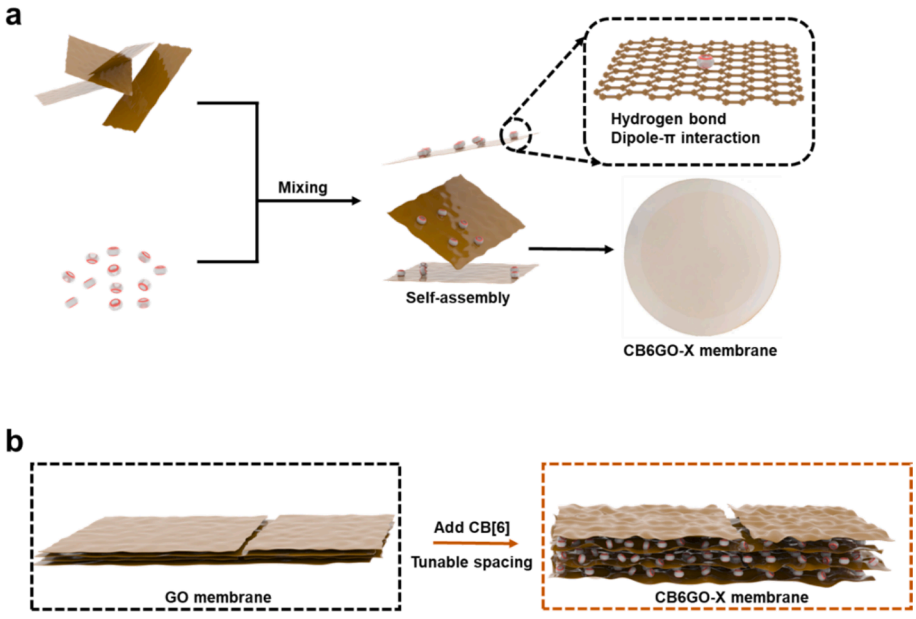

Fig. 1. (a) Schematic diagram of the fabrication process of the CB6GO-X membranes. (b) Schematic illustration of interlayer distance control in GO-based membranes using CB[6] macrocycles.

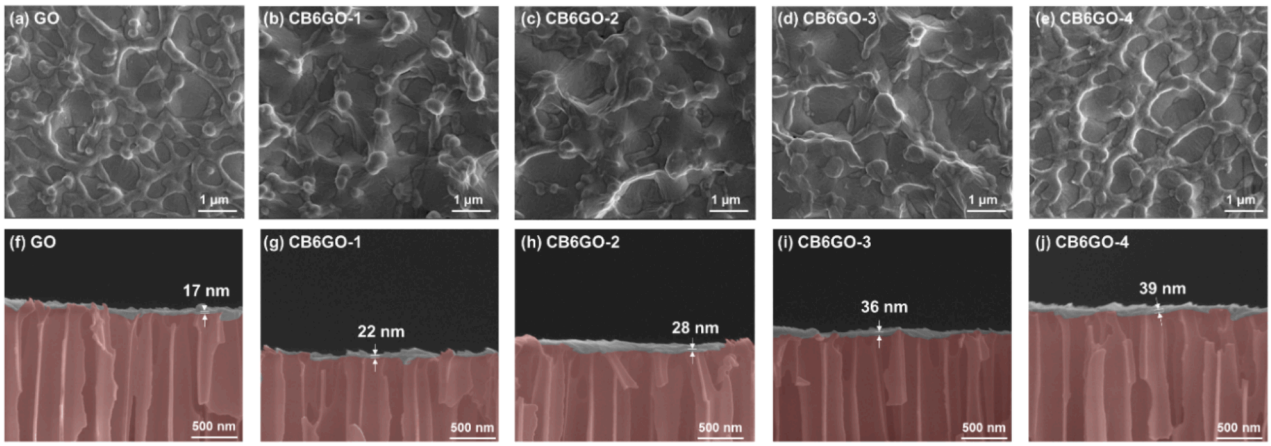

Fig. 2. SEM images of the pure GO membrane and CB6GO-X membranes. (a)-(e) Surface section. (f)-(j) Cross-section. The substrate membranes were artificially colorized.

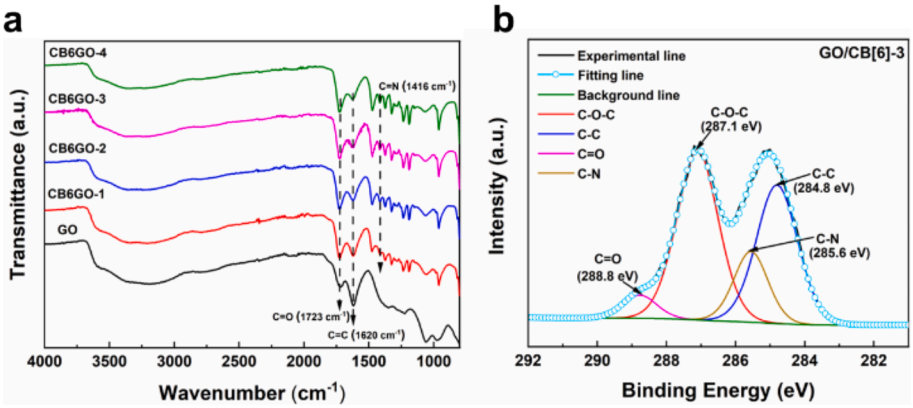

Fig. 3. (a) ATR-FTIR spectra of the pure GO membrane and CB6GO-X membranes. (b) C 1 s (XPS) of the CB6GO-3 membrane.

enabling controlled expansion of the interlayer space to a range (the average interlayer space of the CB6GO-X (X = 1, 2, 3, 4, 5) membranes are 0.69 nm, 0.97 nm, 1.26 nm 1.35 nm and 1.35 nm, respectively). This scenario assumes that CB[6] molecules form a monolayer on the GO surface and function as pillars to support and enlarge the interlayer space. According to the XRD results, the interlayer space in the CB[6]/GO-X membrane increases with the CB[6] content. Notably, both the CB6GO-4 and the CB6GO-5 membranes achieve a maximum interlayer space of 1.35 nm, indicating a consistent structural configuration between the CB6GO-4 and CB6GO-5 membranes. This observation indicates that evaluating membranes with a higher CB[6] loading content in GO than that in CB6GO-4 is unnecessary, warranting to the exclusion of CB6GO-5 from further characterizations and nanofiltration performance evaluations.

To validate the hypothesis positing that CB[6] assembles as a monolayer on GO sheets, it is crucial to compute the surface area ratio between CB[6] and GO. The specific CB[6] content present in the CB6GO-X membranes, as determined from TGA results (Figure S7), is outlined as follows: CB6GO-1 comprises 11.1 wt%, CB6GO-2 comprises 26.9 wt%, CB6GO-3 comprises 40.3 wt%, CB6GO-4 comprises 49.9 wt %, and CB6GO-5 comprises 65.3 wt% of CB[6], respectively, as shown in Fig. 4d. The surface area ratio of CB[6] to GO is calculated by equations S4, S5, and S6. As shown in Fig. 4d, the surface area ratios for the CB6GO-1 to CB6GO-5 membranes are 0.83 %, 2.0 %, 3.02 %, 3.75 %, and 4.90 %, respectively. Given that all recorded values are below 100 %, it is affirmed that CB[6] is insufficient to form a multilayer in GO layers; rather, it disperses as monolayers across the surfaces of GO nanosheets.

The expansion of interlayer spacing within the GO membranes leads to a substantial enhancement in water flux. As depicted in Fig. 4e, the pure water flux (PWF) of the pure GO membrane stands at 28.8 L $m^{-2}h^{-1}$ bar^{-1}. As the loading content of CB[6] increases, there is a notable expansion in the interlayer separation, leading to a substantial rise in PWF, varying from 37.1 to 171.3 L $m^{-2}h^{-1}$ bar^{-1}. Fig. 4f schematically depicts the mechanism through which CB[6] intercalation contributes to the augmentation of PWF.

Molecular dynamics simulations are employed to ascertain the binding conformation of CB[6] to the graphene nanosheets. The detailed results are presented in Table. S1 and Figure S8-S11. It is important to note that graphene is chosen over graphene oxide in these simulations. This decision is based on the acknowledged heterogeneity of the graphene oxide surface, which could lead to significant discrepancies between the binding environment used in the simulations and that in the experimental conditions. As such, native graphene, predominantly unoxidized, is employed for the simulation system [61]. The calculated binding energy of CB[6] to graphene is -400 ± 10 kJ/mol when the CB[6] is intercalated in a parallel orientation between the graphene layers, with the portals of CB[6] perpendicular to the graphene xy plane. In contrast, the binding energy is -340 ± 20 kJ/mol when the CB[6] is intercalated in a perpendicular orientation to and between the graphene layers. Based on these binding energy results, it can be deduced that the parallel orientation of CB[6] relative to the graphene surface is more favourable than the perpendicular configuration. The interlayer distance of graphene layers is measured at 0.35 ± 0.02 nm without intercalation, expanding to 1.15 ± 0.02 nm when CB[6] is aligned parallel to the graphene layers, and further increasing to 1.36 ± 0.05 nm when CB

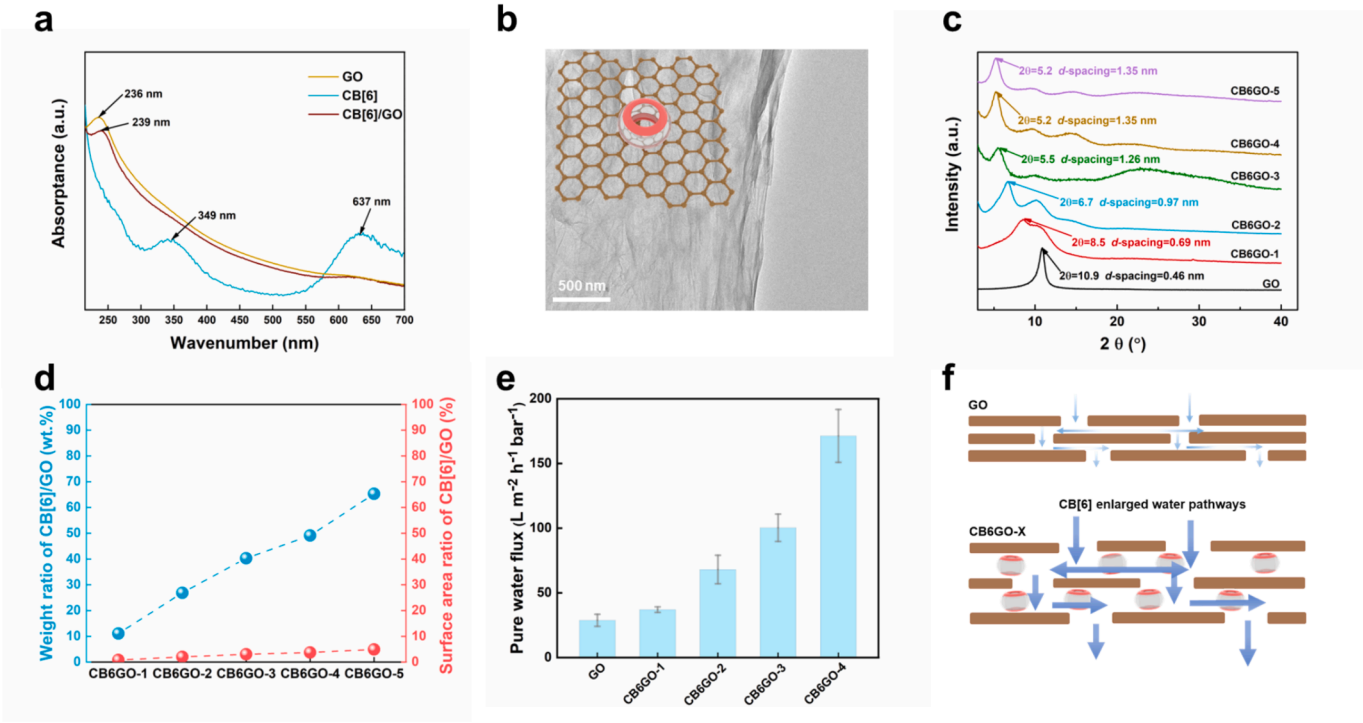

Fig. 4. (a) The UV–vis spectra of GO, CB[6] and CB[6]/GO composite. (b) TEM image of CB[6]/GO nanocomposite. (c)The XRD spectra of the pure GO membrane and CB6GO-X membranes. (d) The actual weight ratio of CB[6]/GO and the estimated surface area ratio of CB[6]/GO of CB6GO-X membranes. (e) Pure water flux of the as-prepared membranes. (f) Schematic illustration of the function of CB[6] in enlarging the water transport channels.

[6] is situated perpendicularly between the graphene layers (Fig. 5). These simulated interlayer distances align well with the experimental results, with CB[6] producing a 0.80 ± 0.04 nm increase in interlayer spacing in the, most favourable, parallel configuration. This finding further supports the hypothesis that CB[6] can effectively regulate the interlayer spacing within the experimentally observed range of 0.46 nm to 1.35 nm (the difference is 0.89 nm). Furthermore, the simulation result reinforces the hypothesis that CB[6] assembles as a monolayer on the GO surface, serving as pillars to expand the interlayer spacing. The binding energy to a single graphene layer is, likewise, −204 ± 3 kJ/mol for the parallel CB[6] orientation and −183 ± 5 kJ/mol for the perpendicular orientation, approximately half the intercalated values, as would be expected. The binding affinity of CB[6] to the graphene surface is over double the value calculated for another common intercalator, ZnO, at −96.5 kJ/mol. This suggests that CB[6] can establish a more stable assembly on the GO surface compared to alternative intercalators [62].

3.3. Separation performance of CB6GO-X membranes

The separation performance is a critical metric for nanofiltration membranes. A high-performance nanofiltration membrane should demonstrate both a high water flux and a high pollutant rejection ratio concurrently. In this study, the GO-based nanofiltration membranes are tested for the removal of organics from industrial saline wastewater. Four different dye molecules, varying in sizes and charge potentials, have been selected as representative pollutants: Alcian blue (AB, positive charge and ca. 2.55 × 2.61 nm; as measured using Chemdraw), Congo red (CR, negative charge and ca. 0.77 × 2.51 nm), Erichrome black T (EBT, negative charge and ca. 0.81 × 1.49 nm) and Methylene blue (MB, negative charge and ca. 1.72 × 1.87 nm). The nanofiltration performance of these membranes is illustrated in Fig. 6. Fig. 6a shows the PWF and rejection performance of the pure GO membrane with different GO content. With an increase in GO content, the dye rejection ratios improve, while the PWF decreases. Beyond a certain GO content, the increase in dye rejection becomes marginal, yet the PWF continues to decrease to a relatively low value. Notably, at a GO content of 20 μg (on a 47 mm diameter substrate), the rejection ratio for all dyes exceeds 98 %, accompanied by a PWF of 28.8 L $m^{-2}h^{-1}$ bar^{-1}. Based on these results, a GO content of 20 μg is identified as the optimal mass for fabricating the CB6GO-X membranes, achieving a balance between dye rejection efficiency and water flux.

As illustrated in Fig. 6b, as the content of CB[6] increases, the PWF of the CB6GO-X membrane significantly escalates, while the dye rejection ratio remains largely consistent. Specifically, at a CB[6] content of 15 μg, corresponding to the CB6GO-3 membrane, it achieves a PWF of 100.3 L $m^{-2}h^{-1}$ bar^{-1}, which is 5.9 times higher than that of the pure GO membrane, while maintaining a rejection ratio of all dyes over 93 %. With a further increase in the CB[6] content, the CB6GO-4 membrane reaches a maximum PWF of 171.3 L $m^{-2}h^{-1}$ bar^{-1}. Nevertheless, this configuration shows a minor decline in the rejection ratio of MB (92 %), due to the larger interlayer distance between the GO nanosheets, though the rejection ratios for the other three dyes remain above 98 %. The relationship between the content of CB[6] and the PWF of the CB6GO-X membrane is attributed to the role of CB[6] molecules as “pillars” in expanding the interlayer distance of the membranes, thereby enhancing water flux without sufficiently widening the gaps to allow dye molecules to pass through (Fig. 6c). This indicates that the largest GO interlayer distance remains smaller than the size of the dye molecules.

Considering the optimal balance between the dye rejection ratio and the PWF, the CB6GO-3 membrane is selected as the representative sample for further evaluation of separation performances under various conditions. As before, AB, CR, EBT and MB are chosen as simulated wastewater pollutants to demonstrate the separation performance. Fig. 7 shows the UV–vis spectra and digital photos of the concentrate, feed and filtrate dye solution of the CB6GO-3 membrane. The concentrated forms of all dyes exhibit a darker hue than the feed, and the UV–vis spectra indicate a higher concentration compared to the feed, even after being diluted twentyfold with water. These findings suggest that dye molecules are obstructed by the CB6GO-3 membrane and

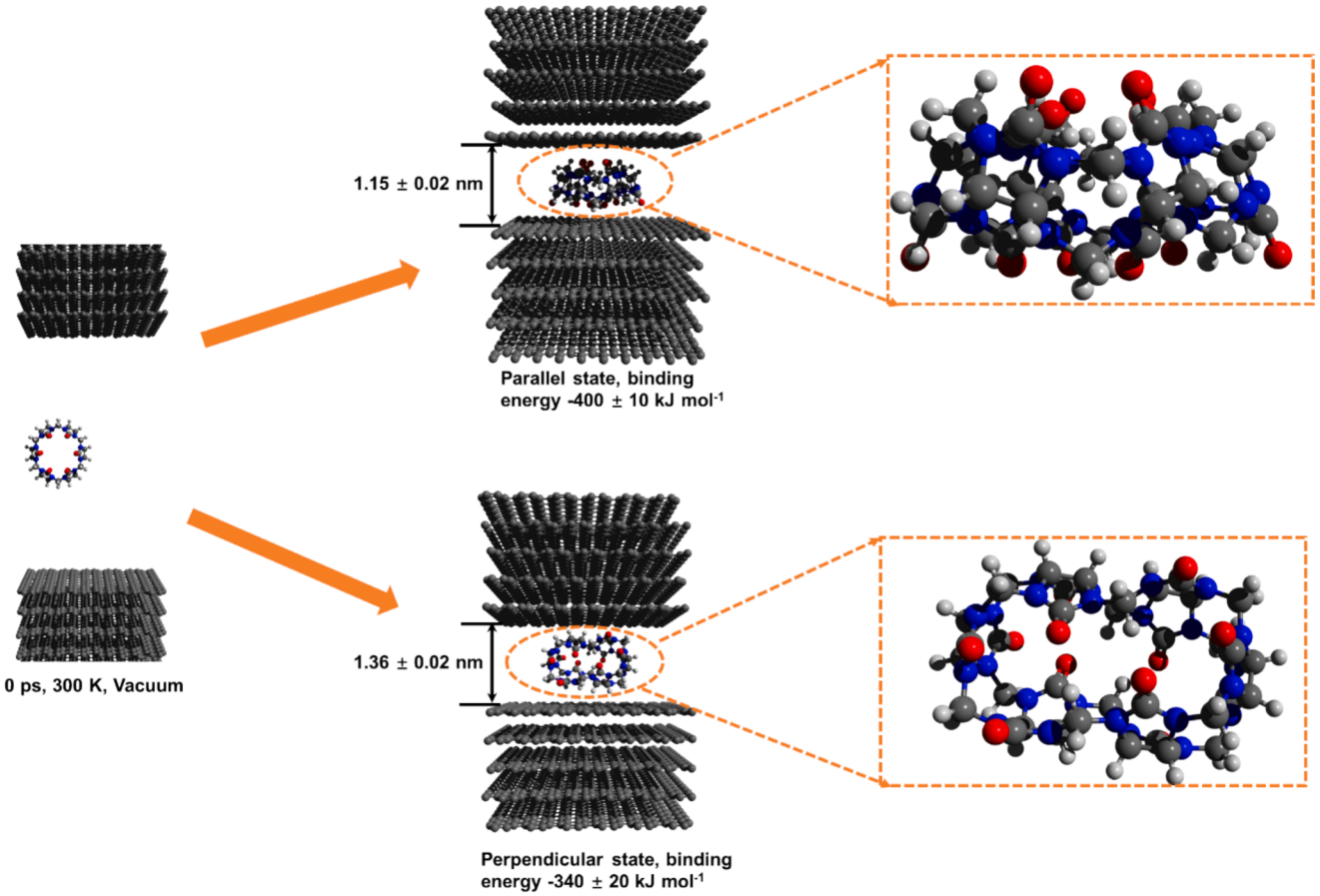

Fig. 5. Process of simulations for CB[6] intercalation between 5 layers of graphene both with no restraints (top) and restraints of 100 N applied in the xy plane for the carbons in the CB[6] backbone. From left to right: The starting point for the simulations, the results of the simulations and a magnified view of the CB[6] structure between the layers.

remain in the solution, indicating that the separation performance is achieved through filtration and rejection, rather than adsorption by the membrane.

Previous studies indicate that membranes fabricated from two-dimensional materials often experience a rapid decline in flux under high pressure due to the compaction of the two-dimensional nanosheets. [63] However, as shown in Fig. 8a, the pure water permeance of the CB6GO-3 membrane remains consistent across a pressure range from 0.5 to 4 bar, and similar stability is observed when the pressure is reversed from 4 to 0.5 bar. This stable PWF under varying pressure indicates that CB6GO-X membranes effectively counteract the typical decline in water permeance caused by the compaction of GO nanosheets. Notably, the permeance of the CB6GO-3 increases in a linear fashion with applied pressure, underscoring the role of CB[6] in maintaining the interlayer distance even under high pressure. This behaviour is attributed to the robust structure of CB[6] molecules, which reinforces the durability and effectiveness of CB[6] in nanofiltration membrane applications.

Reusability is a critical attribute for industrial application of nanofiltration membranes. In this study, CR is utilized as the simulated wastewater pollutant for assessing the reusability of the CB6GO-3 membrane. The membrane's effectiveness is systematically evaluated for CR rejection, with washing in deionized water conducted before each test. As shown in Fig. 8b, after 40 cycles, the CB6GO-3 membrane sustains over 94 % of its initial PWF and retains more than 98 % of its original CR dye rejection ratio. Furthermore, the long-term stability of the CB6GO-3 membrane is evaluated using a crossflow filtration system, a method typically unsuitable for GO-based membranes due to their tendency to disassemble because of the poor interactions between the GO nanosheets. Nonetheless, the CB6GO-3 membrane remains intact within the crossflow cell, likely due to the extra dipole-π conjugation between CB[6] and GO nanosheets as discussed in the previous section. As depicted in Fig. 8c, during a 190-h evaluation period, the CR dye rejection ratio remains constant, while the PWF drops to 46 % of the original value. Fig. 8d compares the performance of CB6GO-3 and CB6GO-4 membranes with other reported GO-based nanofiltration membranes. The CB6GO-3 membrane and the CB6GO-4 membrane present remarkable performance.

The stability of GO and CB6GO-3 membrane was evaluated by soaked the membranes in to water with different pH. As shown in Figure S13, both the GO and the CB6GO-3 could maintain the integrity in acidic (pH = 1) and neutral (pH = 7) water solution. But the GO membrane starts to show delamination after soaking in basic (pH = 13) solution for one day, while the CB6GO-3 membrane can keep the integrity for two weeks, indicating the CB6GO-3 membrane has better stability. Same results are also observed in the ultrasonic treatment. Both the GO membrane and the CB6GO-3 membrane can keep integrity for 200 min under the ultrasonic treatment. They start to peel off from 200 min but the CB6GO-3 membrane shows less delamination than the GO membrane. The improved stability of the CB6GO-3 membrane can be ascribed to the strong dipole-π interaction between the CB[6] and the GO nanosheets, which is also identified by the strong binding energy obtained form the simulation results.

Removing organic waste from saline water is a crucial component in the treatment of industrial wastewater. Based on the size-sieving mechanism, the rejection ratio for salt ions such as Mg^{2+} (0.86 nm), SO_4^{2-} (0.76 nm), Na^{+} (0.72 nm) and Cl^{-} (0.66 nm) is expected to be low, as their diameters are smaller than the interlayer distance of the CB6GO-3 membrane. Consequently, high selectivity between dyes is anticipated.

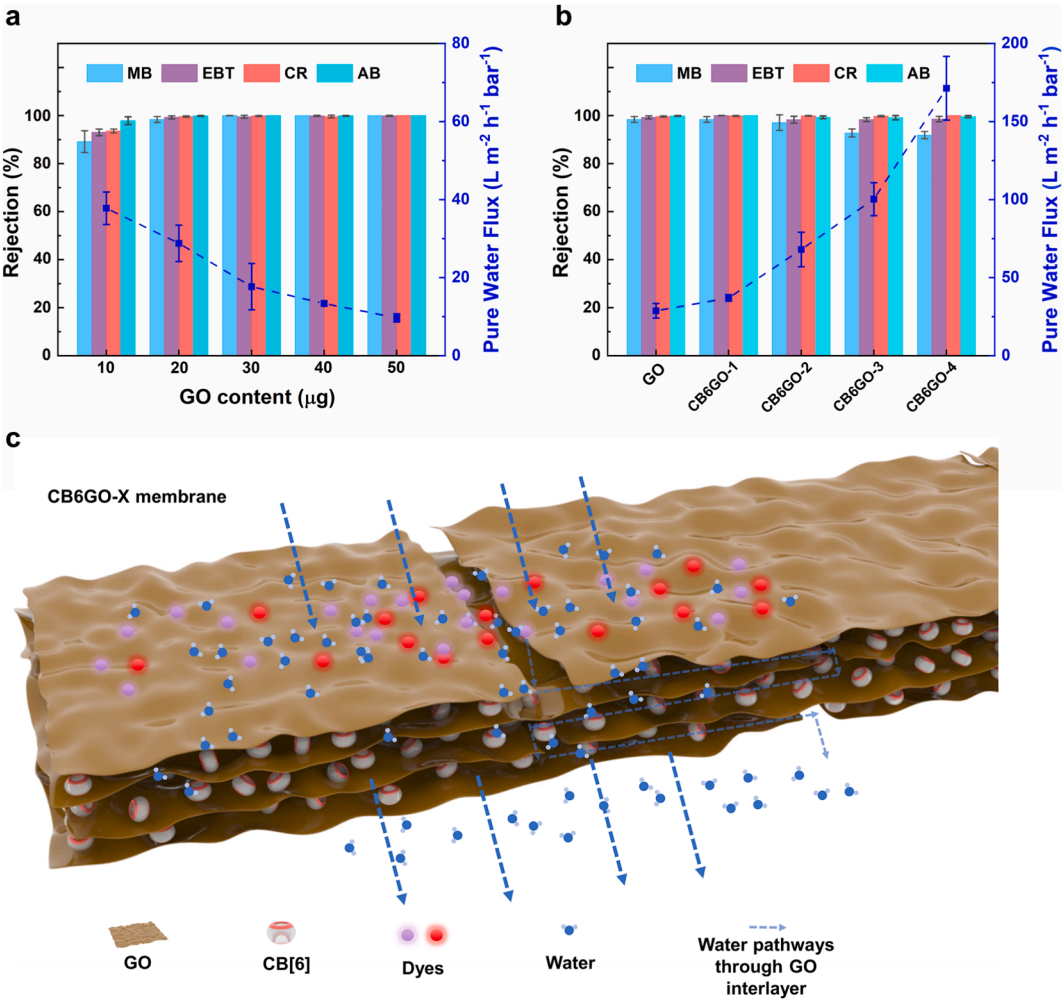

Fig. 6. Flux and dyes rejection performance of (a) pure GO membranes with different amounts of GO nanosheets and (b) CB6GO-X membranes. (c) Schematic transport pathways in CB6GO-X membranes.

Table. S2 reveals that in a single salt solution, the salt permeance ratio for $MgCl_2$, NaCl, $MgSO_4$, and Na_2SO_4 is 98.7 %, 96.4 %, 93.6 %, and 85.1 %, respectively. The order of the salt permeation can be attributed to the Donnan effect,[64–66] where ions sharing the same charge as the membrane are repelled, whereas oppositely charged ions are attracted and thus more likely to pass through the membrane. This phenomenon enables the membrane to effectively separate dyes from salts, with a higher repulsion of multivalent anions and a greater attraction to multivalent cations. The negatively charged CB6GO-3 (-43.1 ± 0.2 mV) membrane exhibits a permeance ratio order of $MgCl_2 > NaCl > MgSO_4 > Na_2SO_4$, influenced by both size-sieving and the Donnan effect. As depicted in Table. 1, the desalination performance of CB6GO-3 is assessed using both single and mixed salt solutions; $MgCl_2$ is chosen as the representative salt with AB and CR as the dye pollutants. In the mixed system with $MgCl_2$, the permeation of AB and CR slightly decreases compared to single dye solutions, likely due to some aggregation of dye molecules, which impedes the permeation of both salt ions and dye molecules. However, the impact of this aggregation is minimal as the distance between the GO sheets, controlling the permeation of salt ions and dyes, is sufficiently large to enable through any salt ions and repel any dye molecules. As the result shows, the permeance of $MgCl_2$ is still maintained at a relatively high level. This outcome highlights the efficacy of CB6GO-X membranes in achieving selective salt/dye separation, offering prospects for removing organics from saline wastewater.

4. Conclusion

In conclusion, CB[6] molecules are assembled onto the GO nanosheets via dipole-π conjugation and subsequently integrated into membranes using a vacuum-assisted self-assembly method. The resultant CB[6]-intercalated GO membranes (CB6GO-X membranes, where X ranges from 1 to 5 to indicate the progressive increase in the weight fraction of CB[6] within the sample) exhibit superior nanofiltration performance. The incorporation of CB[6] molecules as “pillars” in between the GO nanosheets leads to accurate control over the expansion of the interlayer distance, facilitating enhanced water flux while maintaining selective permeability of dye molecules. This phenomenon effectively mitigates the inherent trade-off between pure water flux (PWF) and rejection ratio. Specifically, the CB6GO-4 membrane shows a maximum PWF (171.3 L $m^{-2}h^{-1}$ bar^{-1}) while consistently maintaining a dye rejection performance exceeding 92 % for various dyes with molecular sizes ranging from 1 to 3 nm. Furthermore, the optimized interlayer distance within CB6GO-3 enables ultrahigh dye/salt separation selectivity, reaching up to 761.4. These CB6GO-X membranes leverage the unique properties of the porous macrocyclic molecule CB[6] to address the challenge of low water flux commonly associated with compactly stacked GO nanosheets in traditional GO-based membranes. This innovative and straightforward approach not only demonstrates the potential of CB[6] in enhancing membrane performance but also paves the way for further exploration of macrocyclic molecules in the development of high-performance nanofiltration membranes.

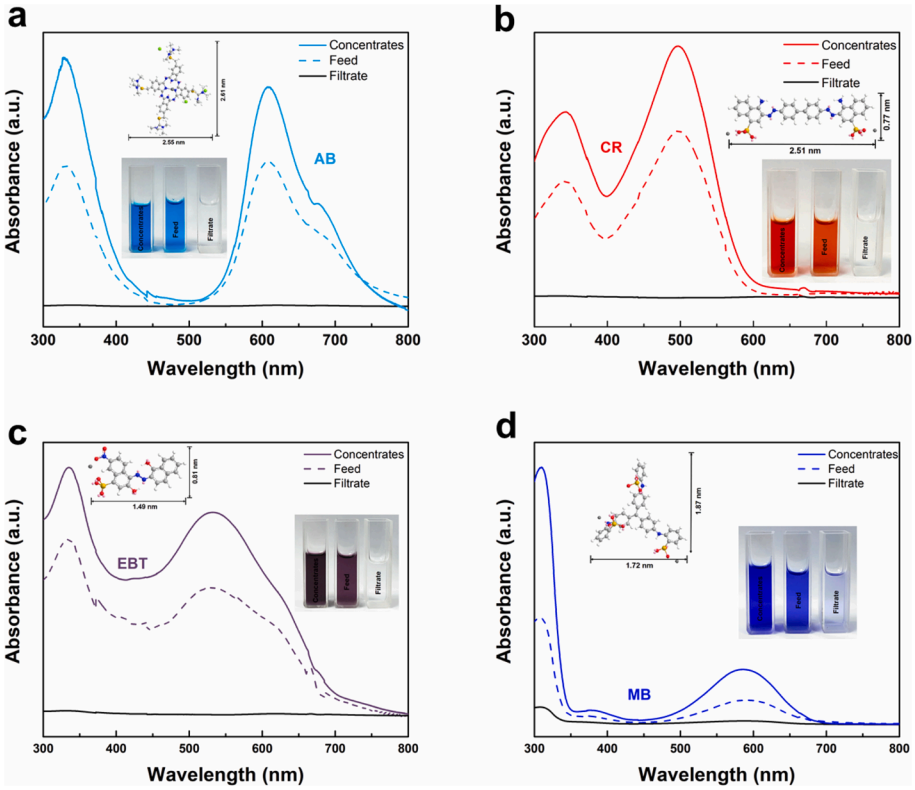

Fig. 7. UV spectra of dyes, (a) AB, (b) CR, (c) EBT and (d) MB with digital photos of concentrates, feed and filtrate.

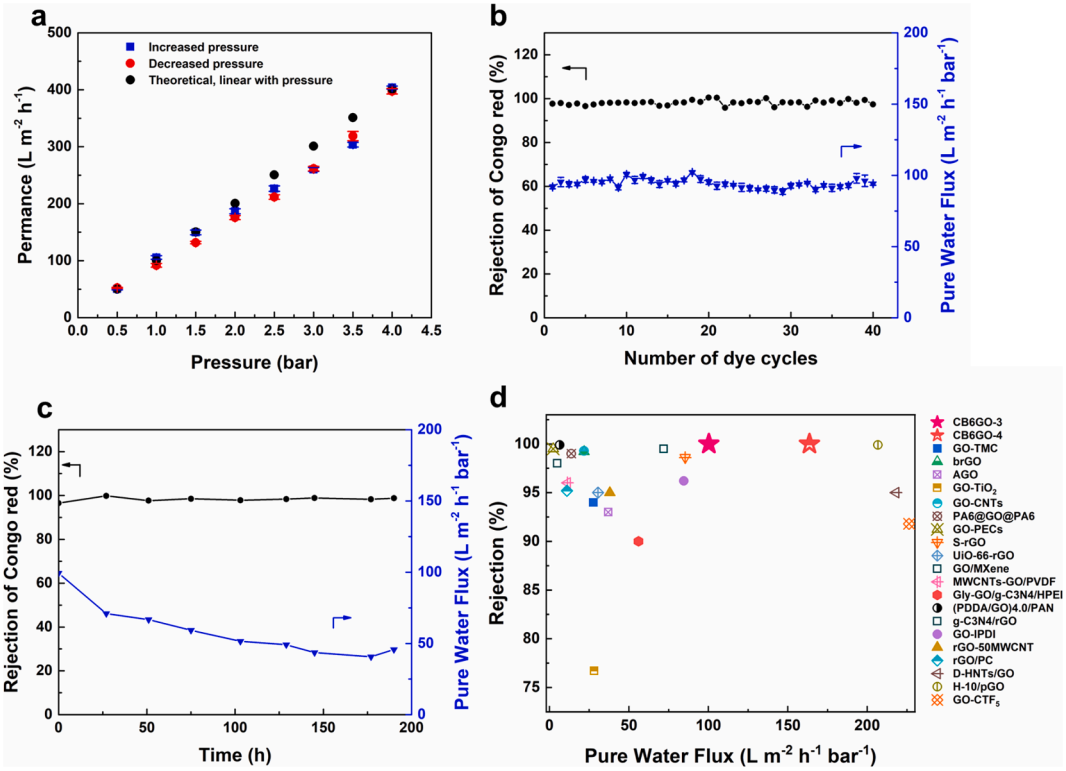

Fig. 8. (a) Permeance of the CB6GO-3 membrane at different pressures. (b) Pure water flux and CR rejection ratio of the CB6GO-3 membrane up to 40 cycles of cleaning. (h) Long-term stability of the CB6GO-3 membrane on a crossflow unit. (d) Separation performances of CB6GO-3 and CB6GO-4 membrane in this work compared with other reported references.

Table 1
Dye/salt separation performance in a single solution and mixed solution.

	Salt	Permeation (%)	Dye	Permeation (%)	Selectivity
Single component	$MgCl_2$	98.7	AB	0.89	111.5
	$MgCl_2$	98.7	CR	0.26	381.5
Mixed solution	$MgCl_2$	93.8	AB	0.12	761.4
	$MgCl_2$	95.7	CR	0.23	423.8

CRediT authorship contribution statement

Pengfei Yang: Writing – review & editing, Writing – original draft, Validation, Resources, Project administration, Methodology, Investigation, Formal analysis, Data curation, Conceptualization. **Yanan Liu:** Writing – review & editing, Validation, Project administration, Formal analysis, Conceptualization. **Gowan-Hugh Whalley:** Writing – review & editing, Writing – original draft, Software, Methodology. **Chengzhi Guo:** Data curation. **Ya Li:** Methodology. **A.Ozgur Yazaydin:** Writing – review & editing, Supervision, Software, Methodology, Data curation. **Zhongyi Jiang:** Writing – review & editing, Supervision, Project administration. **Marc-Olivier Coppens:** Writing – review & editing, Validation, Supervision, Formal analysis. **Yang Lan:** Writing – review & editing, Validation, Supervision, Project administration, Funding acquisition, Formal analysis, Conceptualization.

Declaration of competing interest

The authors declare that they have no known competing financial interests or personal relationships that could have appeared to influence the work reported in this paper.

Acknowledgments

Y. Lan gratefully acknowledges the funding from the Royal Society (RGS/R2/202203Lan_4824933). We also appreciate Dr. Jamie Gould for the XRD tests. M.-O. Coppens thanks the EPSRC Frontier Engineering: Progression Grant; G. Whalley thanks the EPSRC DTP scholarship.

Appendix A. Supplementary data

Supplementary data to this article can be found online at https://doi.org/10.1016/j.cej.2024.158137.

Data availability

Data will be made available on request.

References

[1] M. Elimelech, A. Phillip William, The future of seawater desalination: energy, technology, and the environment, Science 333 (2011) 712–717.
[2] M.A. Shannon, P.W. Bohn, M. Elimelech, J.G. Georgiadis, B.J. Mariñas, A. M. Mayes, Science and technology for water purification in the coming decades, Nature 452 (2008) 301–310.
[3] L. Shiyin, S. Wenxin, S. Yongping, L. Gang, Glacier changes since the Little Ice Age maximum in the western Qilian Shan, northwest China, and consequences of glacier runoff for water supply, J. Glaciol. 49 (2003) 117–124.
[4] P. Singh, L. Bengtsson, Impact of warmer climate on melt and evaporation for the rainfed, snowfed and glacierfed basins in the Himalayan region, J. Hydrol. 300 (2005) 140–154.
[5] S. Gao, Y. Zhu, Y. Gong, Z. Wang, W. Fang, J. Jin, Ultrathin Polyamide Nanofiltration Membrane Fabricated on Brush-Painted Single-Walled Carbon Nanotube Network Support for Ion Sieving, ACS Nano 13 (2019) 5278–5290.
[6] Y. Li, X. You, R. Li, Y. Li, C. Yang, M. Long, R. Zhang, Y. Su, Z. Jiang, Loosening ultrathin polyamide nanofilms through alkali hydrolysis for high-permselective nanofiltration, J. Membr. Sci. 637 (2021) 119623.
[7] A.W. Mohammad, Y.H. Teow, W.L. Ang, Y.T. Chung, D.L. Oatley-Radcliffe, N. Hilal, Nanofiltration membranes review: Recent advances and future prospects, Desalination 356 (2015) 226–254.
[8] C. Yang, Y. Li, M. Long, P. Yang, Y. Li, Y. Zheng, R. Zhang, Y. Su, H. Wu, Z. Jiang, Ultrathin nanofiltration membrane assembled by polyethyleneimine-grafted graphene quantum dots, J. Membr. Sci. 642 (2022) 119944.
[9] D.R. Dreyer, S. Park, C.W. Bielawski, R.S. Ruoff, The chemistry of graphene oxide, Chem. Soc. Rev. 39 (2010) 228–240.
[10] W. Fei, M. Xue, H. Qiu, W. Guo, Heterogeneous graphene oxide membrane for rectified ion transport, Nanoscale 11 (2019) 1313–1318.
[11] J. Guan, X. You, B. Shi, Y. Liu, J. Yuan, C. Yang, X. Pang, H. Wu, J. Shen, C. Fan, M. Long, R. Zhang, Z. Jiang, Engineering multi-pathway graphene oxide membranes toward ultrafast water purification, J. Membr. Sci. 638 (2021) 119706.
[12] N.A. Khan, J. Yuan, H. Wu, L. Cao, R. Zhang, Y. Liu, L. Li, A.U. Rahman, R. Kasher, Z. Jiang, Mixed nanosheet membranes assembled from chemically grafted graphene oxide and covalent organic frameworks for ultra-high water flux, ACS Appl. Mater. Interface. 11 (2019) 28978–28986.
[13] R.R. Nair, H.A. Wu, P.N. Jayaram, I.V. Grigorieva, A.K. Geim, Unimpeded permeation of water through helium-leak tight graphene-based membranes, Science 335 (2012) 442–444.
[14] Z.P. Smith, B.D. Freeman, Graphene oxide: a new platform for high-performance gas- and liquid-separation membranes, Angew. Chem. Int. Ed. 53 (2014) 10286–10288.
[15] Y. Zhu, S. Murali, W. Cai, X. Li, J.W. Suk, J.R. Potts, R.S. Ruoff, Graphene and graphene oxide: synthesis, properties, and applications, Adv. Mater. 22 (2010) 3906–3924.
[16] Q. Guo, M. Xu, Q. Tang, Y. Liu, W. Zhang, C. Guo, X. Zhao, Y. Zhu, S. Ye, D. Liu, W. Lei, C. Chen, Advanced hybrid nanosheet membranes with stable nanochannels for ultrafast molecular separation, npj Clean Water 6 (2023) 38.
[17] M. Xu, Q. Tang, Y. Liu, J. Shi, W. Zhang, C. Guo, Q. Liu, W. Lei, C. Chen, Charged boron nitride nanosheet membranes for improved organic solvent nanofiltration, Acs Appl. Mater. Interface 15 (2023) 12524–12533.
[18] W. Geng, Z. Zhang, Q. Guo, Y. Liu, X. Ye, H. Zhang, C. Fu, F. Liu, Y. Zhu, C. Chen, Tailoring graphene oxide nanofiltration membrane with adjustable nanochannels for enhanced molecule separation, Chem. Eng. J. 478 (2023) 147327.
[19] B. Mi, Graphene oxide membranes for ionic and molecular sieving, Science 343 (2014) 740–742.
[20] S.P. Koenig, L. Wang, J. Pellegrino, J.S. Bunch, Selective molecular sieving through porous graphene, Nat. Nanotechnol. 7 (2012) 728–732.
[21] L. Fei, C. Chen, L. Shen, Y. Zhang, B. Wang, J. Xu, B. Li, S. Raza, H. Lin, Graphene oxide assisted assembly of superhydrophilic MOF-based membrane with 2D/3D hybrid nanochannels for enhanced water purification, Chem. Eng. J. 460 (2023) 141694.
[22] B. Wang, L. Shen, J. Xu, L. Fei, B. Li, H. Lin, C. Chen, Spiropyran molecular aggregates implanted photo-responsive graphene oxide membrane with self-cleaning ability for enhanced water purification, J. Membr. Sci. 702 (2024) 122744.
[23] B. Wang, L. Shen, Y. He, C. Chen, Z. Yang, L. Fei, J. Xu, B. Li, H. Lin, Covalent Organic Framework/Graphene Hybrids: Synthesis, Properties, and Applications, Small 20 (2024) 2310174.
[24] Y. Ma, Y. Su, M. He, B. Shi, R. Zhang, J. Shen, Z. Jiang, Graphene oxide membranes with conical nanochannels for ultrafast water transport, ACS Appl. Mater. Interface. 10 (2018) 37489–37497.
[25] Y. Liu, J. Guan, Y. Su, R. Zhang, J. Cao, M. He, J. Yuan, F. Wang, X. You, Z. Jiang, Graphene oxide membranes with an ultra-large interlayer distance through vertically grown covalent organic framework nanosheets, J. Mater. Chem. a. 7 (2019) 25458–25466.
[26] D.W. Kim, J. Choi, D. Kim, H.-T. Jung, Enhanced water permeation based on nanoporous multilayer graphene membranes: the role of pore size and density, J. Mater. Chem. A. 4 (2016) 17773–17781.
[27] Y. Liu, M.-O. Coppens, Cell membrane-inspired graphene nanomesh membrane for fast separation of oil-in-water emulsions, Adv. Funct. Mater. 32 (2022) 2200199.
[28] M. Zhang, K. Guan, Y. Ji, G. Liu, W. Jin, N. Xu, Controllable ion transport by surface-charged graphene oxide membrane, Nat. Commun. 10 (2019) 1253.
[29] C. Xu, Y. Xu, J. Zhu, Photocatalytic antifouling graphene oxide-mediated hierarchical filtration membranes with potential applications on water purification, ACS Appl. Mater. Interface. 6 (2014) 16117–16123.
[30] Y. Liu, Y. Su, J. Guan, J. Cao, R. Zhang, M. He, K. Gao, L. Zhou, Z. Jiang, 2D heterostructure membranes with sunlight-driven self-cleaning ability for highly efficient oil–water separation, Adv. Funct. Mater. 28 (2018) 1706545.
[31] R.L.G. Lecaros, A.R. Matira, L.L. Tayo, W.-S. Hung, C.-C. Hu, H.-A. Tsai, K.-R. Lee, J.-Y. Lai, Homostructured graphene oxide-graphene quantum dots nanocomposite-based membranes with tunable interlayer spacing for the purification of butanol, Sep. Purif. Technol. 283 (2022) 120166.
[32] L. Zhang, Y. Lu, Y.-L. Liu, M. Li, H.-Y. Zhao, L.-A. Hou, High flux MWCNTs-interlinked GO hybrid membranes survived in cross-flow filtration for the treatment of strontium-containing wastewater, J. Hazard. Mater. 320 (2016) 187–193.
[33] C.-Y. Wang, W.-J. Zeng, T.-T. Jiang, X. Chen, X.-L. Zhang, Incorporating attapulgite nanorods into graphene oxide nanofiltration membranes for efficient dyes wastewater treatment, Sep. Purif. Technol. 214 (2019) 21–30.
[34] X. Sui, Z. Yuan, C. Liu, L. Wei, M. Xu, F. Liu, A. Montoya, K. Goh, Y. Chen, Graphene oxide laminates intercalated with 2D covalent-organic frameworks as a robust nanofiltration membrane, J. Mater. Chem. A. 8 (2020) 9713–9725.
[35] Y. Ying, D. Liu, W. Zhang, J. Ma, H. Huang, Q. Yang, C. Zhong, High-flux graphene oxide membranes intercalated by metal–organic framework with highly selective separation of aqueous organic solution, ACS Appl. Mater. Interface. 9 (2017) 1710–1718.

[36] A. He, Z. Jiang, Y. Wu, H. Hussain, J. Rawle, M.E. Briggs, M.A. Little, A. G. Livingston, A.I. Cooper, A smart and responsive crystalline porous organic cage membrane with switchable pore apertures for graded molecular sieving, Nat. Mater. 21 (2022) 463–470.
[37] Z. Jiang, R. Dong, A.M. Evans, N. Biere, M.A. Ebrahim, S. Li, D. Anselmetti, W. R. Dichtel, A.G. Livingston, Aligned macrocycle pores in ultrathin films for accurate molecular sieving, Nature 609 (2022) 58–64.
[38] S.J. Barrow, S. Kasera, M.J. Rowland, J. del Barrio, O.A. Scherman, Cucurbituril-based molecular recognition, Chem. Rev. 115 (2015) 12320–12406.
[39] J. Kim, I.-S. Jung, S.-Y. Kim, E. Lee, J.-K. Kang, S. Sakamoto, K. Yamaguchi, K. Kim, New cucurbituril homologues: syntheses, isolation, characterization, and X-ray crystal structures of cucurbit[n]uril (n = 5, 7, and 8), J. Am. Chem. Soc. 122 (2000) 540–541.
[40] P. Zhang, Y. Zhang, L. Wang, K. Qiu, X. Tang, J.K. Gibson, X. Liu, L. Mei, S. An, Z. Huang, P. Ren, Y. Wang, Z. Chai, W. Shi, Bioinspired macrocyclic molecule supported two-dimensional lamellar membrane with robust interlayer structure for high-efficiency nanofiltration, Adv. Sci. 10 (2023) 2206516.
[41] L.F. Villalobos, T. Huang, K.-V. Peinemann, Cyclodextrin films with fast solvent transport and shape-selective permeability, Adv. Mater. 29 (2017) 1606641.
[42] X. Mao, M. Xu, H. Wu, X. He, B. Shi, L. Cao, P. Yang, M. Qiu, H. Geng, Z. Jiang, Supramolecular Calix[n]arenes-intercalated graphene oxide membranes for efficient proton conduction, ACS Appl. Mater. Interface. 11 (2019) 42250–42260.
[43] P. Yang, H. Wu, N.A. Khan, B. Shi, X. He, L. Cao, X. Mao, R. Zhao, M. Qiu, Z. Jiang, Intrinsic proton conductive deoxyribonucleic acid (DNA) intercalated graphene oxide membrane for high-efficiency proton conduction, J. Membr. Sci. 606 (2020) 118136.
[44] M.-J. Tang, M.-L. Liu, D.-A. Wang, D.-D. Shao, H.-J. Wang, Z. Cui, X.-L. Cao, S.-P. Sun, Precisely patterned nanostrand surface of cucurbituril[n]-based nanofiltration membranes for effective alcohol–water condensation, Nano Lett. 20 (2020) 2717–2723.
[45] J. Cai, X.-L. Cao, Y. Zhao, F.-Y. Zhou, Z. Cui, Y. Wang, S.-P. Sun, The establishment of high-performance anti-fouling nanofiltration membranes via cooperation of annular supramolecular Cucurbit[6]uril and dendritic polyamidoamine, J. Membr. Sci. 600 (2020) 117863.
[46] X.-L. Cao, J.-L. Guo, J. Cai, M.-L. Liu, S. Japip, W. Xing, S.-P. Sun, The encouraging improvement of polyamide nanofiltration membrane by cucurbituril-based host–guest chemistry, AICHE J. 66 (2020) e16879.
[47] K. Baek, D. Xu, J. Murray, S. Kim, K. Kim, Permselective 2D-polymer-based membrane tuneable by host–guest chemistry, Chem. Commun. 52 (2016) 9676–9678.
[48] J. Lee, F. Zhou, K. Baek, W. Kim, H. Su, K. Kim, R. Wang, T.-H. Bae, Use of rigid cucurbit[6]uril mediating selective water transport as a potential remedy to improve the permselectivity and durability of reverse osmosis membranes, J. Membr. Sci. 623 (2021) 119017.
[49] M. Wu, M. Zhang, L. Shen, X. Wang, D. Ying, H. Lin, R. Li, Y. Xu, H. Hong, High propensity of membrane fouling and the underlying mechanisms in a membrane bioreactor during occurrence of sludge bulking, Water Res. 229 (2023) 119456.
[50] Y. Long, G. Yu, L. Dong, Y. Xu, H. Lin, Y. Deng, X. You, L. Yang, B.-Q. Liao, Synergistic fouling behaviors and mechanisms of calcium ions and polyaluminum chloride associated with alginate solution in coagulation-ultrafiltration (UF) process, Water Res. 189 (2021) 116665.
[51] Z. Wang, Y. Zeng, Q. Tan, Y. Shen, L. Shen, J. Sun, L. Zhao, H. Lin, Novel combination of iron-carbon composite and Fenton oxidation processes for high-concentration antibiotic wastewater treatment, J. Environ. Manage. 354 (2024) 120383.
[52] J. Yu, L. Zhang, L. Shen, R. Li, D. Zhao, H. Lin, Y. Xu, Y. Jiao, In situ grown cyclodextrin metal-organic framework nanoparticles templated stripe nano-wrinkled polyamide nanofiltration membranes for efficient desalination and antibiotic removal, J. Membr. Sci. 694 (2024) 122413.
[53] M. Yabe, K. Mori, K. Ueda, M. Takeda, Development of PolyParGen software to facilitate the determination of molecular dynamics simulation parameters for polymers, J. Comput. Chem. Japan –Internat. Ed. 5 (2019).
[54] S. Dasetty, J.K. Barrows, S. Sarupria, Adsorption of amino acids on graphene: assessment of current force fields, Soft Matter 15 (2019) 2359–2372.
[55] H. Tang, D. Liu, Y. Zhao, X. Yang, J. Lu, F. Cui, Molecular dynamics study of the aggregation process of graphene oxide in water, J. Phys. Chem. C 119 (2015) 26712–26718.
[56] P. Avouris, C. Dimitrakopoulos, Graphene: synthesis and applications, Mater. Today 15 (2012) 86–97.
[57] A. Wagner, K.H. Ly, N. Heidary, I. Szabó, T. Földes, K.I. Assaf, S.J. Barrow, K. Sokołowski, M. Al-Hada, N. Kornienko, M.F. Kuehnel, E. Rosta, I. Zebger, W. M. Nau, O.A. Scherman, E. Reisner, Host–guest chemistry meets electrocatalysis: cucurbit[6]uril on a Au surface as a hybrid system in CO2 reduction, ACS Catal. 10 (2020) 751–761.
[58] T.F. Emiru, D.W. Ayele, Controlled synthesis, characterization and reduction of graphene oxide: A convenient method for large scale production, Egypt. J. Basic Appl. Sci. 4 (2017) 74–79.
[59] Z. Çiplak, N. Yildiz, A. Çalimli, Investigation of graphene/ag nanocomposites synthesis parameters for two different synthesis methods, Fuller. Nanotub. Car. n. 23 (2015) 361–370.
[60] Y. Sheng, X. Tang, E. Peng, J. Xue, Graphene oxide based fluorescent nanocomposites for cellular imaging, J. Mater. Chem. b. 1 (2013) 512–521.
[61] E. Aliyev, V. Filiz, M.M. Khan, Y.J. Lee, C. Abetz, V. Abetz, Structural characterization of graphene oxide: surface functional groups and fractionated oxidative debris, Nanomaterials (basel) 9 (2019).
[62] Z. Liu, D. Ge, P. Yang, Structure and interfacial properties investigation for ZnO/graphene interface, Mater. Chem. Phys. 229 (2019) 1–5.
[63] Y. Wei, Y. Zhang, X. Gao, Y. Yuan, B. Su, C. Gao, Declining flux and narrowing nanochannels under wrinkles of compacted graphene oxide nanofiltration membranes, Carbon 108 (2016) 568–575.
[64] S. Sarkar, A.K. SenGupta, P. Prakash, The donnan membrane principle: opportunities for sustainable engineered processes and materials, Environ. Sci. Technol. 44 (2010) 1161–1166.
[65] P.-Y. Pontalier, A. Ismail, M. Ghoul, Mechanisms for the selective rejection of solutes in nanofiltration membranes, Sep. Purif. Technol. 12 (1997) 175–181.
[66] B. Chaufer, M. Rabiller-Baudry, L. Guihard, G. Daufin, Retention of ions in nanofiltration at various ionic strength, Desalination 104 (1996) 37–46.